J. Mech. Phys. Solids 180 (2023) 105417

Contents lists available at ScienceDirect

Journal of the Mechanics and Physics of Solids

journal homepage: www.elsevier.com/locate/jmps

Microstructurally-sensitive fatigue crack nucleation in a Zircaloy-4 alloy

Weifeng Wan [a,b], Yilun Xu [b,c,*], Xikai Yu [d], Fionn P.E. Dunne [b]

[a] School of Energy and Power Engineering, Beihang University, Beijing 100191, China
[b] Department of Materials, Royal School of Mines, Imperial College London, SW7 2AZ, UK
[c] Institute of High Performance Computing (IHPC), Agency for Science, Technology and Research (A*STAR), 1 Fusionopolis Way, #16-16 Connexis, Singapore 138632, Republic of Singapore
[d] Department of Mechanical Engineering, Imperial College London, SW7 2AZ, UK

ARTICLE INFO

Keywords:
Fatigue crack nucleation
Zirconium alloy
Microstructures
Stored energy density
Crystal plasticity finite element

ABSTRACT

Microstructurally-sensitive fatigue crack nucleation and subsequently short crack growth were observed at an edge-notch in a textured Zircaloy-4 sample with the c-axis aligned perpendicular to the viewing surface. To understand the competition between the main crack and the secondary crack nucleation at the edge-notch root, a combined experimental and computational investigation was conducted to analyse various micro-scale mechanical quantities, including local strain, local stress, GND density, and stored energy density. A computational crystal plasticity finite element simulation that incorporated grain morphology, crystallographic orientation, and loading conditions was found to have good agreement with experimental results from the three-point bend fatigue test. The results showed that both the main crack and secondary crack nucleation sites had the highest magnitudes of local stored energy density, indicating that this factor was both necessary and sufficient for crack nucleation.

1. Introduction

Zirconium alloys are extensively utilised in nuclear reactors as fuel claddings and pressure tubes due to their exceptional ductility, corrosion high resistance, and low cross-section to thermal neutrons (Nielsen and Wilfing, 2012). The constant power fluctuations in a nuclear reactor core result in periodic swelling and shrinking of the fuel pellets, leading to cyclic loads on the zircaloy claddings. As a result, fatigue fractures can be a mode of failure for these components. Fatigue crack nucleation is a crucial stage in the formation of cracks and is considered to be an incubation process before the crack becomes physically observable. A significant fraction of the total fatigue life is taken up by fatigue crack nucleation and subsequently short crack growth (Suresh, 1998; Suresh and Ritchie, 1984), making a deep understanding of fatigue crack nucleation imperative for the development of more accurate fatigue life prediction methods.

The mechanism of fatigue crack nucleation in ductile materials has been studied extensively in the past decades. Cyclic loads generate dislocations that move due to irreversible slip (Suresh, 1998). The fatigue slip bands lead to 'roughening' of the material surface (Forsyth, 1953; Cottrell and Hull, 1957; Wood, 1958). After continued cyclic stresses, these dislocations move irreversibly and pile up to form persistent slip bands (PSBs) (Stroh, 1954; Tanaka and Mura, 1982; Thompson et al., 1956). Further studies with

* Corresponding author.
E-mail addresses: yilun.xu@imperial.ac.uk, xu_yilun@ihpc.a-star.edu.sg (Y. Xu).

https://doi.org/10.1016/j.jmps.2023.105417
Received 6 May 2023; Received in revised form 1 August 2023; Accepted 8 August 2023
Available online 12 August 2023
0022-5096/© 2023 The Author(s). Published by Elsevier Ltd. This is an open access article under the CC BY license (http://creativecommons.org/licenses/by/4.0/).

experimental observations on PSBs show that cyclic strain localisation within PSBs roughens sample surface and acts as fatigue crack nucleation site (Brown, 2013; Cheng and Laird, 1981; Ho et al., 2015; Sauzay and Gilormini, 2002). A good review of PSBs formation as a precursor to fatigue crack nucleation can be found in Man et al. (2009).

It has been clear that the highly heterogeneous nature of the development of slip, and its dependence on microstructural features such as grain boundaries and crystallographic orientations are associated with fatigue crack nucleation (Castelluccio et al., 2014). Dislocations tend to pile up at grain boundaries with larger lattice misorientations, in which the fatigue crack nucleation is more likely to occur (Miao et al., 2012). Recent studies on the interaction between grain boundaries and PSBs led to an energy-based criterion of PSB structure for fatigue crack nucleation (Sangid et al., 2011). Experimental study by Littlewood and Wilkinson (2012) indicated that cracks nucleate at grains with high strain concentration, influenced strongly by the direction of crystallographic c-axis in a Ti-6Al-4V alloy. Similarly, microtextured regions which were favourably orientated for basal or prism slip were found to act as crack nucleation sites in a titanium alloy (Szczepanski et al., 2013).

Fatigue crack nucleation criteria have been introduced at differing length scales and for relevant microstructural features (Dunne, 2014; Pineau et al., 2016). Stress was firstly considered as a fatigue failure criteria in early studies at the macroscopic scale without consideration of microstructural features (Fatemi and Socie, 1988). Shanthraj and Zikry (2013) proposed a critical fracture stress as fatigue crack nucleation criterion at the microstructural scale. Shear-based parameters such as maximum shear strain were found to correlate well with multiaxial fatigue conditions (Przybyla et al., 2013; Przybyla and McDowell, 2011). A critical accumulated slip was proposed as fatigue crack nucleation criterion in a nickel-base alloy (Dunne et al., 2007b; Manonukul and Dunne, 2004). Sweeney et al. (2013) demonstrated that plastic strain was found to be a necessary but not sufficient condition for fatigue crack nucleation which correlated well with nucleation site.

Mechanistic modelling incorporating fatigue crack nucleation criteria at differing length scales and for relevant microstructural features have been addressed using three key modelling techniques: crystal plasticity finite element (CPFE), discrete dislocation plasticity (DDP), and molecular dynamics (Dunne, 2014). One of the key challenges is to identify the dominant length scales and microstructural features when modelling fatigue in specific materials. At macro- and meso- scales, CPFE is capable of predicting a wide range of fatigue behaviours, which takes into consideration the effect of microstructure heterogeneity to quantify the fatigue response at the microstructural scale. Manonukul and Dunne (2004) proposed a fatigue crack initiation criterion based on a critical accumulated slip by a rate-dependent polycrystal CPFE model, which correctly predicted the fatigue life for both high- and low-cycle fatigue. Hochhalter et al. (2010) developed a CP model and they found a non-local nucleation metric could be used to predict the crack nucleation in AA 7075-T651 alloy. DDP has the advantage and the potential to capture highly localised slip fields which the crystal plasticity approach cannot. A discrete dislocation dynamics model for fatigue crack initiation in a surface grain has been developed by Brinckmann and Van der Giessen (2004). Their model considered dislocations as line singularities where they could be generated from pre-existing sources, glide and annihilate. However, a remaining limitation of the DDP method is its inability to capture core dislocation interactions, and some details of the structure of dislocations such as cells, ladders, veins and stacking faults.

A stored energy criterion has been proposed as a quantitative assessment of the driver of fatigue crack nucleation (Chen et al., 2018, 2017; Wan et al., 2014). Subsequent study by Prastiti et al. (2020) employed discrete dislocation and crystal plasticity to determine stored energy density and dislocation configurational energy with the aim of identifying fatigue crack nucleation site. This stored

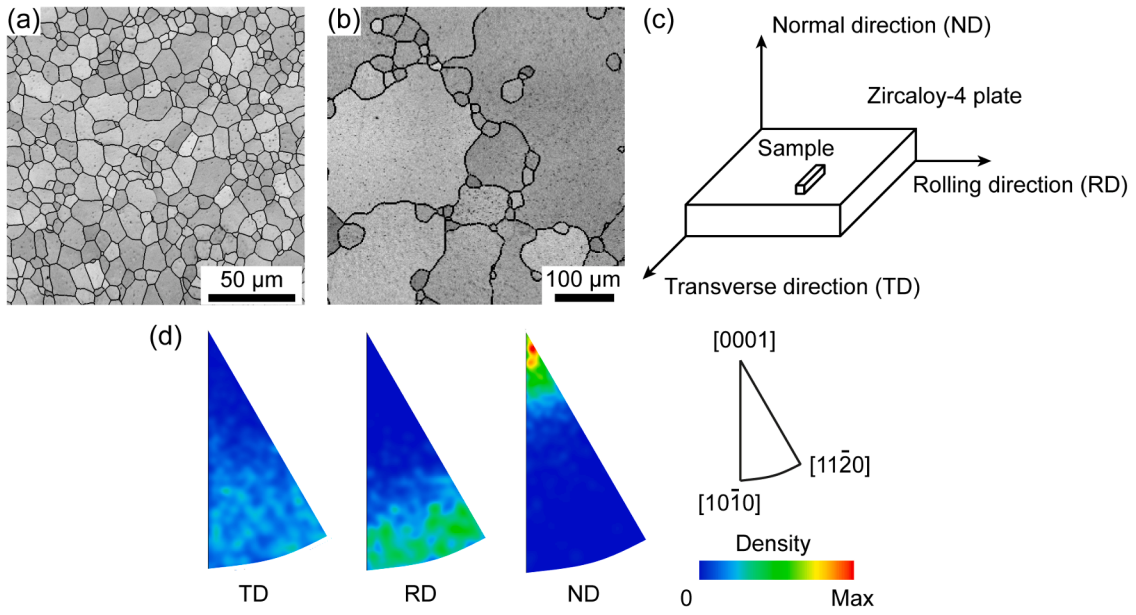


Fig. 1. (a) Fine-grain microstructure in the as-received Zircaloy-4 plate; (b) 'Blocky alpha' microstructure in the heat treated Zircaloy-4 sample; (c) schematic of beam samples cutting from Zircaloy-4 plate; (d) pole figures showing strong basal texture in HCP Zircaloy-4.

energy density criterion, which has common features with both Griffith fracture energy (Griffith, 1921) and a dislocation-based nucleation argument (Stroh, 1954, 1953), unifies the contributions to fatigue crack nucleation from several microstructural quantities including local slip accumulation, local stress, local strain and dislocation density. Chen et al. (2017) successfully applied the stored energy density criterion to identify the fatigue crack nucleation site in a group of three-point bend tests on Ni-based single and oligo crystals, in which the primary crack nucleation site and also the second nucleation site were unambiguously captured. Wan et al. (2016) achieved a good prediction of the fatigue life in a polycrystalline Ni alloy by utilising the stored energy density criterion. Recent study by Bergsmo et al. (2022) applied a multi-scale modelling strategy (CPFE-DDP) to assess experimental observation of fatigue crack nucleation site at twin boundaries generating high local stored energy density.

This study provides a direct approach to measure the local stored energy density through experiments and compares the results to CPFE modelling in the context of fatigue crack nucleation in a hexagonal close packed (HCP) Zircaloy-4. The study utilises advanced characterization techniques including electron backscatter diffraction (EBSD) and in situ high-resolution optical digital image correlation (DIC) to address micro-scale quantities including local strain, local stress, geometrically necessary dislocation (GND) density, and stored energy density. The objective of this work is to increase the understanding of fatigue crack nucleation in Zircaloy-4 by integrating state-of-the-art characterization techniques, specifically in situ DIC, with quantitatively validated CPFE simulations.

2. Experimental

2.1. Materials

The as-received Zircaloy-4 plate was in the form of hot-rolled and recrystallised with fine-grain microstructure (average grain size of ~10 μm) as shown in Fig. 1 (a). The fine-grain Zircaloy-4 plate was cut into beam shape samples with nominal dimensions of 12.0 × 3.2 × 3.0 mm^3 by electrical discharge machining. Square section samples were encapsulated in a quartz tube with argon and then heat treated at 800°C for two weeks followed by furnace cooling to generate large grains known as 'blocky alpha' shown in Fig. 1 (b). The EBSD results show that the fine-grain Zircaloy-4 plate has strong basal texture as the c-axes of hexagonal crystals are aligned with the normal direction (ND) (see Fig. 1 (c) and (d)).

2.2. Fatigue test

Low-cycle fatigue was applied by three-point bend tests on Zircaloy-4 beam samples with 'blocky alpha' microstructures. An edge notch was prepared at the bottom centre of the beam sample. The geometries of the beam and notch are shown in Fig. 2 (a) and (b). Fig. 2 (c) shows the schematic of three-point bend testing. The distance between two fixed supports was 10 mm. Force-controlled cyclic load was applied on the top of the beam with stress-ratio of zero (shown in Fig. 2 (d)).

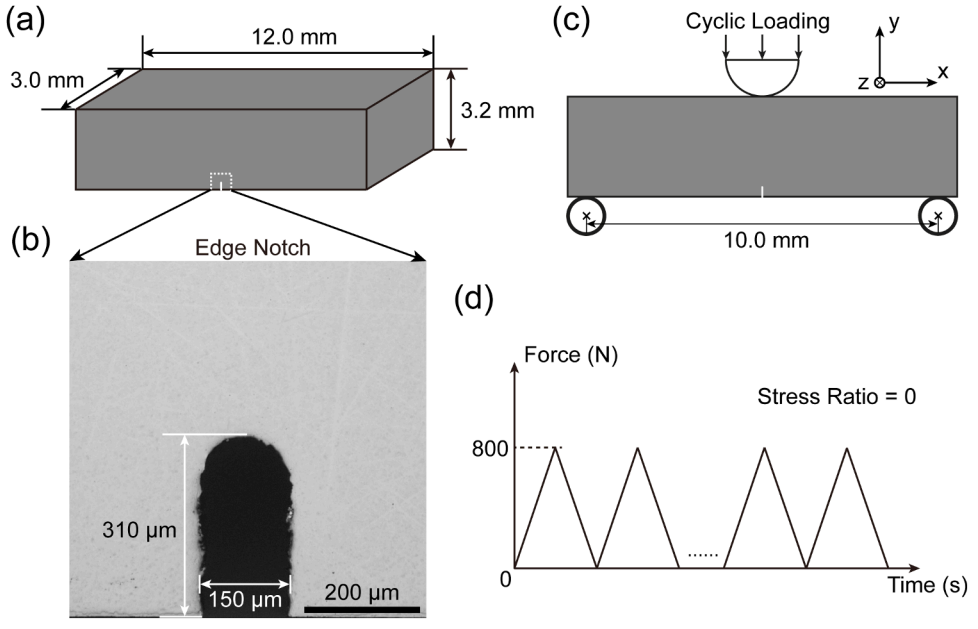


Fig. 2. (a) Schematic of edge-notched Zircolay-4 beam sample; (b) optical image showing the geometry of edge notch; (c) 2D schematic of three-point bend testing on a Zircaloy-4 beam sample; (d) loading history of three-point bend testing.

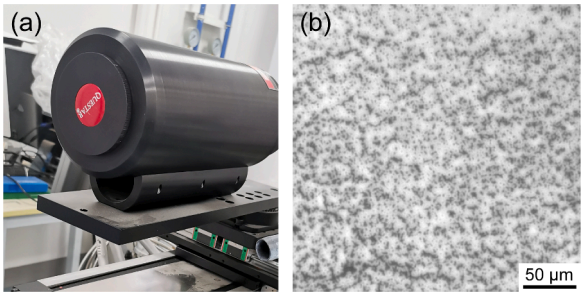


Fig. 3. (a) Questar-100 microscope; (b) digital image correlation speckles on the Zircaloy-4 sample surface.

2.3. In-situ DIC

Optical DIC technology was utilised to measure the in-plane strain fields. An in-situ DIC setup equipped with a Questar-100 microscope (shown in Fig. 3 (a)) and a versatile scientific camera was utilised with three-point bend fatigue testing on a Shimadzu universal testing machine. The details of the arrangement can be found in Xu et al. (2021). Before DIC examination the Zircaloy-4 sample surfaces were coated with diamond speckles (average 1 μm in size) as shown in Fig. 3 (b).

A succession of speckle images were simultaneously captured by the camera with an interval time of 0.5 s when the cyclic three-point bend testing was going on such that the displacement of the speckles were recorded through individual cycles and over many cycles in situ. The speckle pattern pictures were captured in real-time without interrupting the cyclic loading. The interval time (0.5 s) is short enough to capture the beam positions at peak load and in the unloaded condition during a full cycle. The obtained image size was 1392 × 1040 pixels which corresponds to a resolution of around 1 μm per pixel. The field of view is large enough to allow the movement of the region of interest (ROI) to be captured, and cropped later in the image processing. In this way, the images recorded at the peak load and in the unloaded condition were able to be extracted out for the strain calculation by an in-house Matlab code using a cross-correlation algorithm (Jiang et al., 2016). The cross-correlation algorithm was applied in a two-step process to accurately measure the strain: the first step corrected the average rigid body translation and the whole frame rotation of the image within a large subset of 256 × 256 pixels. This was followed by the second stage, which used a 64 × 64 pixel ROI in the cross-correlation analysis with

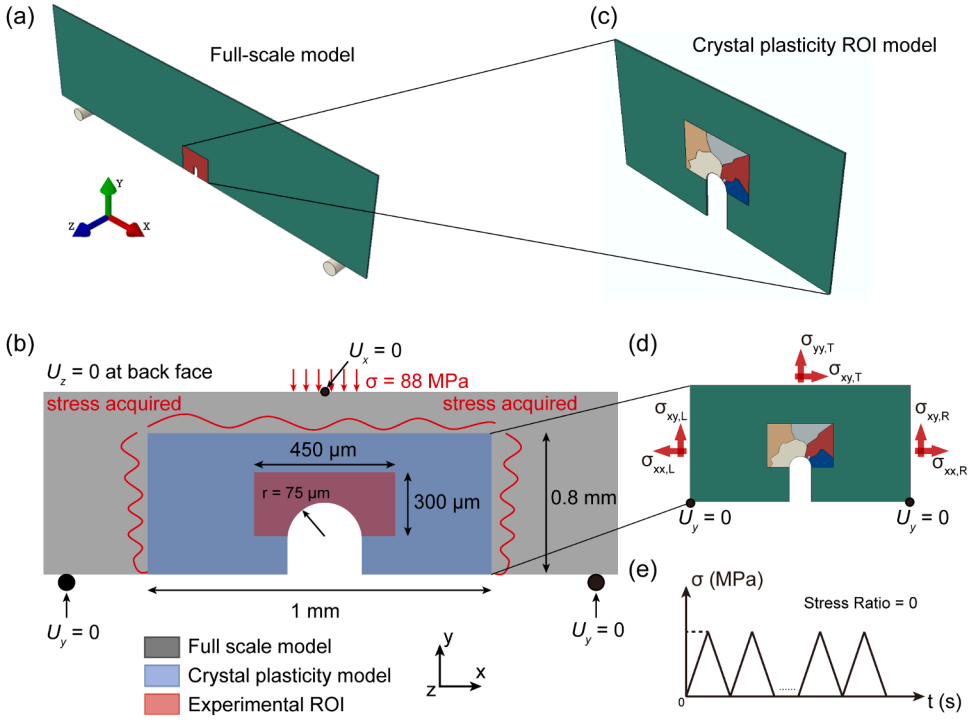


Fig. 4. The multi-scale crystal plasticity models for the three-point bending test for the Zircaloy-4 notched sample: (a) the full-scale model that replicates the test sample dimension; (b) the schematic diagram for the boundary and loading conditions imposed on the full-scale model and the ROI sub-model; the region for EBSD and DIC characterization is also labelled for reference; (c) the ROI sub-model that contains the EBSD region; (d) the sub-model boundary and loading conditions and (e) the remote beam loading conditions imposed on the ROI sub-model.

95% overlap. This ensured a high spatial resolution of the strain measurement, estimated to be ~3 μm. The combination of these two steps allowed for a precise and thorough analysis of the speckled image, yielding accurate results for the strain measurement.

2.4. SEM and EBSD

Materials characterisation was performed using a combination of scanning electron microscope (SEM) and EBSD examination. A Zeiss Sigma-300 SEM equipped with a Bruker EBSD detector was applied to scan over the prepared sample surface. The SEM images were captured at an acceleration voltage of 5 keV during routine SEM imaging. For EBSD analysis, the SEM was operated at an acceleration voltage of 20 keV with the bulk sample tilted 70 degrees from horizontal to ensure proper scanning of the surface.

3. Simulation

3.1. Multi-scale three-point bend model

A multi-scale modelling strategy for the Zircaloy-4 beam was utilized to simulate the notched samples subject to the cyclic three-point bending (Liu et al., 2022). A full-scale model that reproduced the dimensions and boundary conditions of the Zircaloy-4 beam sample was firstly established by considering the material as a single crystal, in order only to determine appropriate boundary conditions for the local micro-scale polycrystal sub-model. This is reasonable because of the strong texture of the polycrystal sample (see Fig.1(d)), shown in Fig. 4 (a). This implementation also improves the computational efficiency without losing much accuracy on extracting the boundary conditions for the micro-scale model. The force loading was applied over a 3 mm-length along the x-direction contact area with a peak pressure $\sigma_{\text{app}} = 88$ MPa (reflecting the total applied load 800 N in the experimental fatigue test), and the displacement constraints in the y-direction were prescribed for both supports ($U_y = 0$), while the back face of the full-scale model sample was constrained along the z-direction ($U_z = 0$). A region with dimensions 1.0 mm × 0.8 mm near the notch (shown in Fig. 4 (b)) was chosen to reflect the EBSD and DIC region of analysis in the experiments. Therefore, the estimated stress distribution was cyclically imposed on the corresponding crystal plasticity ROI sub-model that contained the EBSD region, as shown in Fig. 4 (c) and (d). It is noted that all the stress components (including shears) generated from the macroscale model are imposed at the sub-model boundaries to ensure the faithful boundary conditions for the crystal plasticity ROI sub-model. The distribution of the stress components along the three boundaries for the crystal plasticity ROI sub-model are shown in Appendix A.

3.2. Rate-dependent CPFE modelling

A strain-rate dependent CPFE framework is adopted for the material description in this study. Only a summary is given here, and full details of the framework can be found in Dunne et al. (2007a). The plastic strain rate $\dot{\boldsymbol{\varepsilon}}^{\text{p}}$ is determined from the shear rate $\dot{\gamma}^{(i)}$ along all active slip systems, which gives:

$$\dot{\boldsymbol{\varepsilon}}^{\text{p}} = \sum_{i=1}^{M} \dot{\gamma}^{(i)} \boldsymbol{s}^i \otimes \boldsymbol{n}^i \tag{1}$$

where M is the total number of active slip systems (up to 32 for a HCP crystal), and $\boldsymbol{s}^i$ and $\boldsymbol{n}^i$ are the slip direction and normal direction vectors of the ith slip system, respectively. The slip rate $\dot{\gamma}^{(i)}$ along the ith slip system is governed by thermally activated dislocation escape from obstacles (such as lattice defect, impurities, inclusions, etc), which is given by

$$\dot{\gamma}^{(i)} = \rho_{ssdm} b^2 \nu_D \exp\left(-\frac{\Delta H}{k\theta}\right) \sinh\left(\frac{\Delta V}{k\theta}\left|\tau^{(i)} - \tau_c^{(i)}\right|\right) \tag{2}$$

where ρ_{ssdm} is the mobile statistically stored dislocation (SSD) density, b the Burgers vector, ν_D the frequency of attempted dislocation jump over obstacles, ΔH the activation energy with associated activation volume ΔV, k the Boltzmann constant, and $\tau^{(i)}$ and $\tau_c^{(i)}$ are the resolved shear stress and critical resolved shear stress on the ith slip system, respectively. The critical resolved shear stress, or intrinsic slip system strength, $\tau_c^{(i)}$ evolves with both SSD and GND density, where the former is related to the plastic strain evolution and the

Table 1
HCP Zircaloy-4 material properties for CPFE simulation.

Parameter (unit)	Value	Parameter (unit)	Value
E_{11} (GPa)	98	$\tau_{c0}^{(a)}$ (MPa) - *prism*	153
E_{33} (GPa)	123	$\tau_{c0}^{(a)}$ (*MPa*) - *basal*	204
G_{12} (GPa)	35	$\tau_{c0}^{(c+a)}$ (*MPa*) - *pyramidal*	532
G_{13} (GPa)	32	k (JK^{-1})	1.38×10^{-23}
ν_{12}	0.40	ΔF (eV)	0.31
ν_{13}	0.24	ΔV	$18.8b^3$
b (nm)	0.32	ρ_{ssdm} (μm^{-2})	0.01

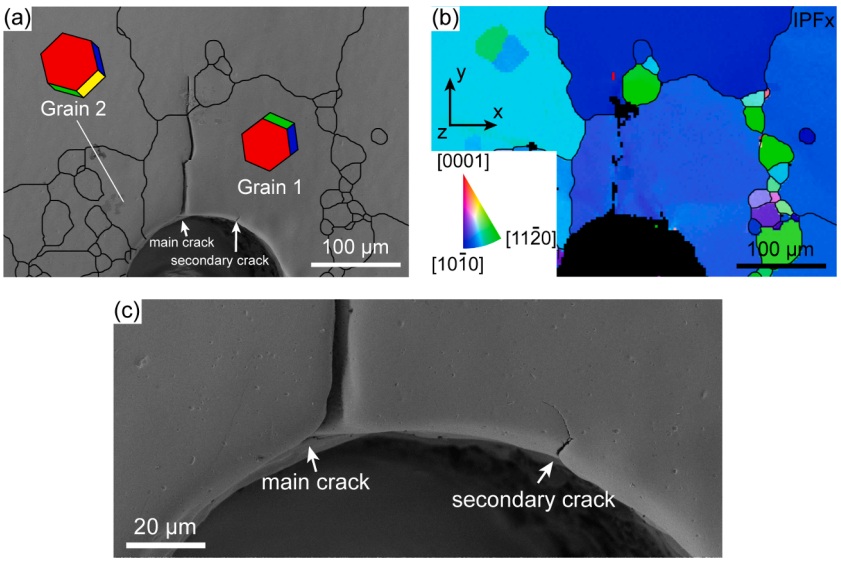


Fig. 5. SEM image (a) and inverse pole figure (IPF) image along the X-direction (b) showing the crack nucleation sites at the notch root and the short crack growth in a heat treated Zircaloy-4 sample with strong basal texture after 1500 cycles;(c) enlarged SEM image of (a).

latter to lattice curvature resulting from plastic strain gradients. The strain rate sensitivity of a slip system is governed by the combination of ΔH and ΔV (Dunne et al., 2007a).

A Taylor-based hardening law is adopted for the evolution of shear resistance along the ith slip system:

$$\tau_c^{(i)} = \tau_{c0}^{(i)} + G_s b\sqrt{\rho_{ssd} + \rho_{gnd}} \tag{3}$$

where $\tau_{c0}^{(i)}$ is the intrinsic critical resolved shear stress, G_s the shear modulus, and ρ_{ssd} and ρ_{gnd} are the density of statistically stored and geometry necessary dislocations respectively. The evolution of SSD density for simplicity is related only to the effective plastic strain p:

$$\dot{\rho}_{ssd} = \lambda\dot{p} \tag{4}$$

where the coefficient λ controls the slip system isotropic hardening rate. The effective plastic strain rate $\dot{p}$ is given by:

$$\dot{p} = \sqrt{\frac{2}{3}\dot{\boldsymbol{\varepsilon}}^{\boldsymbol{p}} : \dot{\boldsymbol{\varepsilon}}^{\boldsymbol{p}}} \tag{5}$$

where $\dot{\boldsymbol{\varepsilon}}^{\boldsymbol{p}}$ is the plastic strain rate.

The components of the GND density tensor are calculated from Nye's dislocation tensor (Nye, 1953) $\boldsymbol{\Lambda}$ that originates from the lattice curvatures given by the curl of the plastic deformation gradient $\boldsymbol{F}^{\boldsymbol{p}}$:

$$\boldsymbol{\Lambda} = \nabla \times \boldsymbol{F}^{\boldsymbol{p}} = \sum_{i=1}^{M} \rho_{Gs}^{i}\boldsymbol{b}^{i} \otimes \boldsymbol{s}^{i} + \rho_{Get}^{i}\boldsymbol{b}^{i} \otimes \boldsymbol{t}^{i} + \rho_{Gen}^{i}\boldsymbol{b}^{i} \otimes \boldsymbol{n}^{i} \tag{6}$$

where ρ_{Gs}^{i} is the screw component, ρ_{Get}^{i} and $\rho_{Gen}^{i}$the edge components, $\boldsymbol{b}^{i}$ the Burgers vector, $\boldsymbol{s}^{i}$, $\boldsymbol{t}^{i}$ and $\boldsymbol{n}^{i}$ the unit vectors on the ith slip system, respectively.

The full form of solving the GND density tensor $\boldsymbol{\rho}_{\mathrm{G}}$ is hence given by:

$$\boldsymbol{A}\boldsymbol{\rho}_{\mathrm{G}} = \overline{\boldsymbol{\Lambda}} \tag{7}$$

where $\overline{\boldsymbol{\Lambda}}$ is the vectorised Nye dislocation tensor, $\boldsymbol{A}$ is a $9 \times (3 \times 32)$ matrix containing the coefficients of the $\boldsymbol{b}^{i} \otimes \boldsymbol{s}^{i}$, $\boldsymbol{b}^{i} \otimes \boldsymbol{t}^{i}$ and $\boldsymbol{b}^{i} \otimes \boldsymbol{n}^{i}$ terms. The 96 independent GND components cannot be uniquely solved with the nine equations alone from the term $\boldsymbol{\Lambda}$. The scalar GND density is hence determined by the L2-norm minimization of the edge and screw dislocation density components of Nye's tensor (Cheng and Ghosh, 2015):

$$\rho_{gnd} = \sqrt{\sum_{i=1}^{M} \left(\rho_{Gs}^{i}\right)^2 + \left(\rho_{Get}^{i}\right)^2 + \left(\rho_{Gen}^{i}\right)^2} \tag{8}$$

The dissipated energy density U is given by:

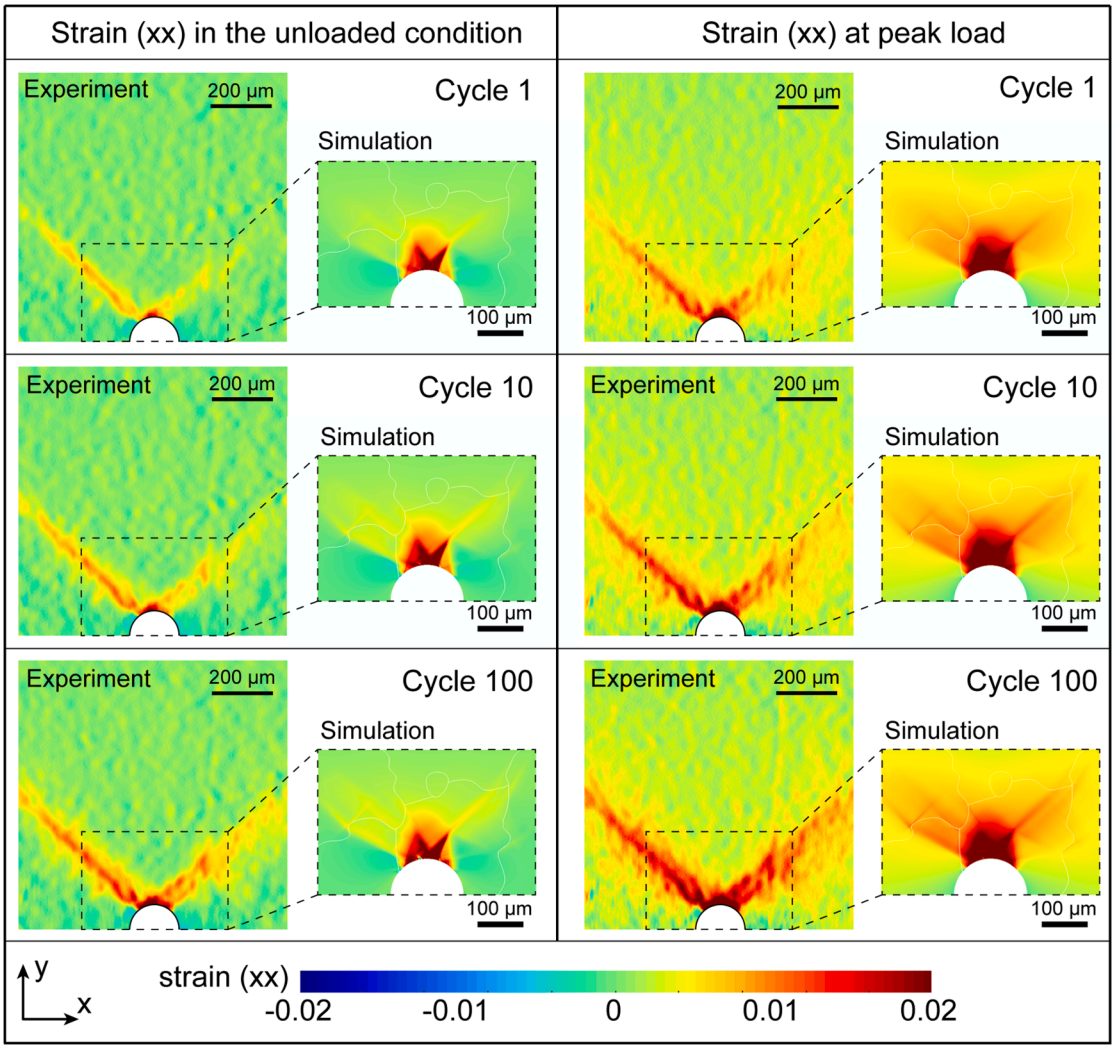


Fig. 6. Experimental and simulation strain (xx) distributions at cycle 1, 10, and 100 in the unloaded condition and at peak load of the Zircaloy-4 sample.

$$U = \int \boldsymbol{\sigma} : d\boldsymbol{\varepsilon}^{p} \tag{9}$$

and the stored energy density G (Wan et al., 2014) is given as:

$$G = \frac{U\Delta V_s}{\Delta A_s} = \int \frac{|\xi\sigma : d\boldsymbol{\epsilon}_p|}{\sqrt{\rho_{ssd} + \rho_{gnd}}} \tag{10}$$

where ξ is the fraction of dissipated energy stored as dislocation structures and estimated to be ~ 0.05 (Kamlah and Haupt). The Zircaloy-4 single crystal material properties used in the CPFE modelling are given in Table 1 and taken from Wilson et al. (2018).

Our gradient-enhanced crystal plasticity framework enables slip accumulation, GND density and SSD density to be determined and allows these quantities to be assessed in the context of the experimental microstructural characterisation of fatigue crack nucleation and early short crack growth.

4. Results and discussion

4.1. Microstructural characterisation

Zircaloy-4 samples after heat treatment exhibited a 'blocky alpha' microstructure with extremely large grain size (> 200 μm), as shown in Fig. 5. The c-axes of crystals in the 'blocky alpha' Zircaloy-4 sample were aligned with the Z-direction, indicating a strong

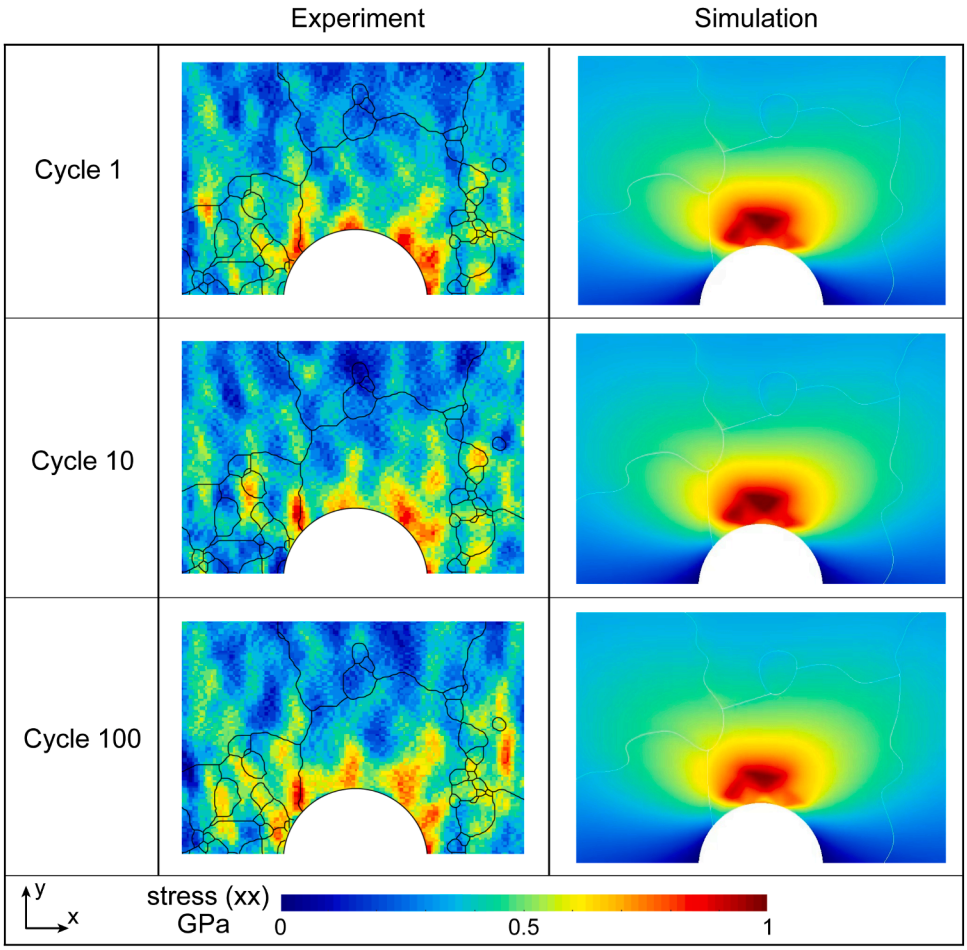


Fig. 7. Experimental and simulation results showing the distributions of stress (xx) in the ROI of the Zircaloy-4 sample at peak load.

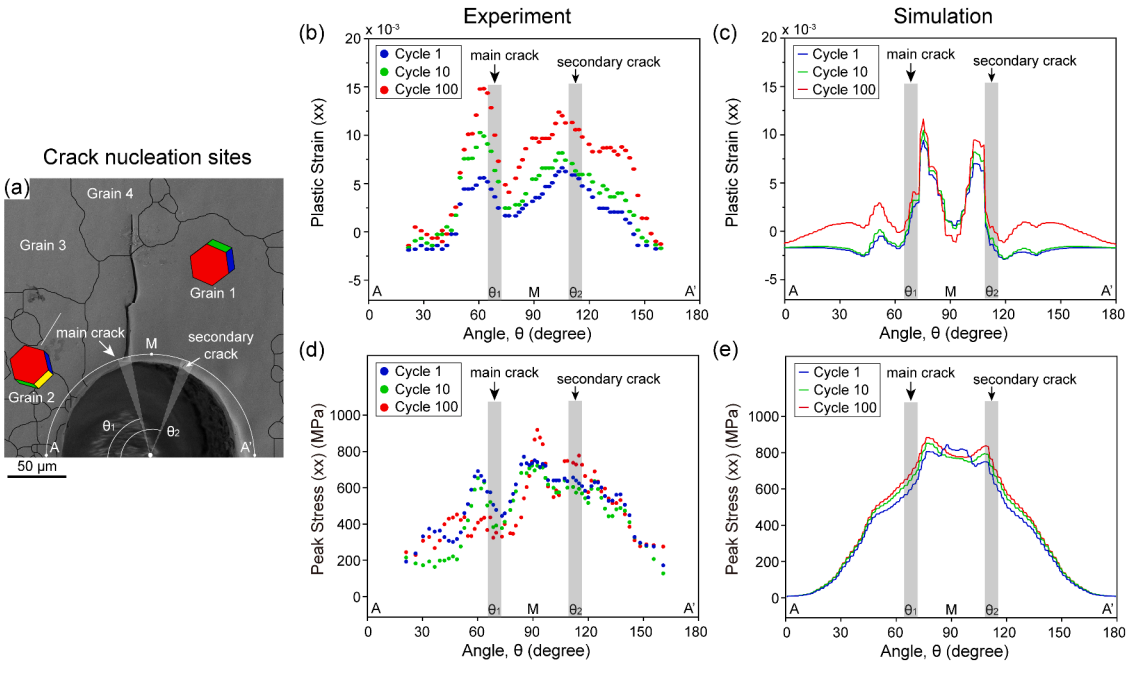


Fig. 8. (a) SEM image showing the crack nucleation sites in the Zircaloy-4 sample; Experimental (b) and simulation (c) results of plastic strain (xx) versus angle along path AMA' in (a); Experimental (d) and simulation (e) results of peak stress (xx) versus angle along path AMA' in (a).

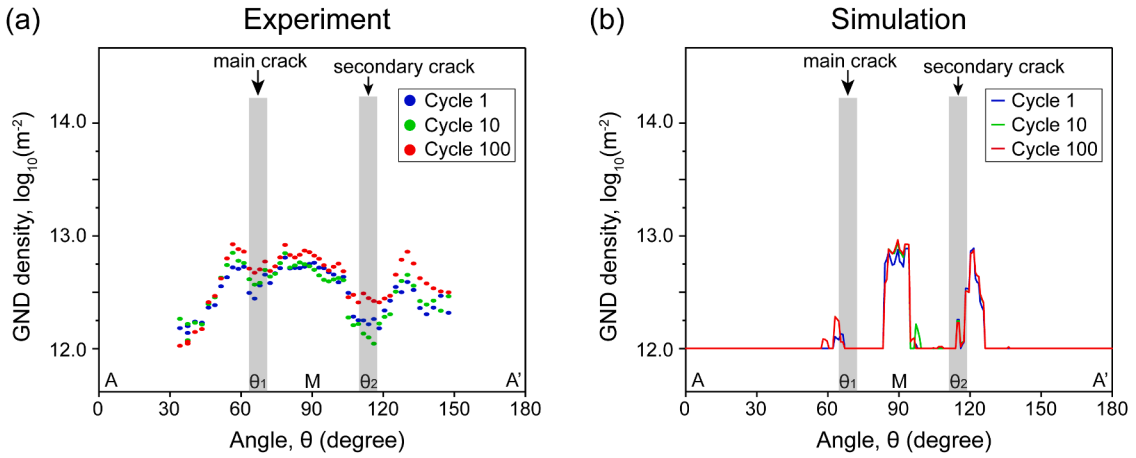


Fig. 9. (a) Experimental and (b) simulation GND density versus angle along path AMA'.

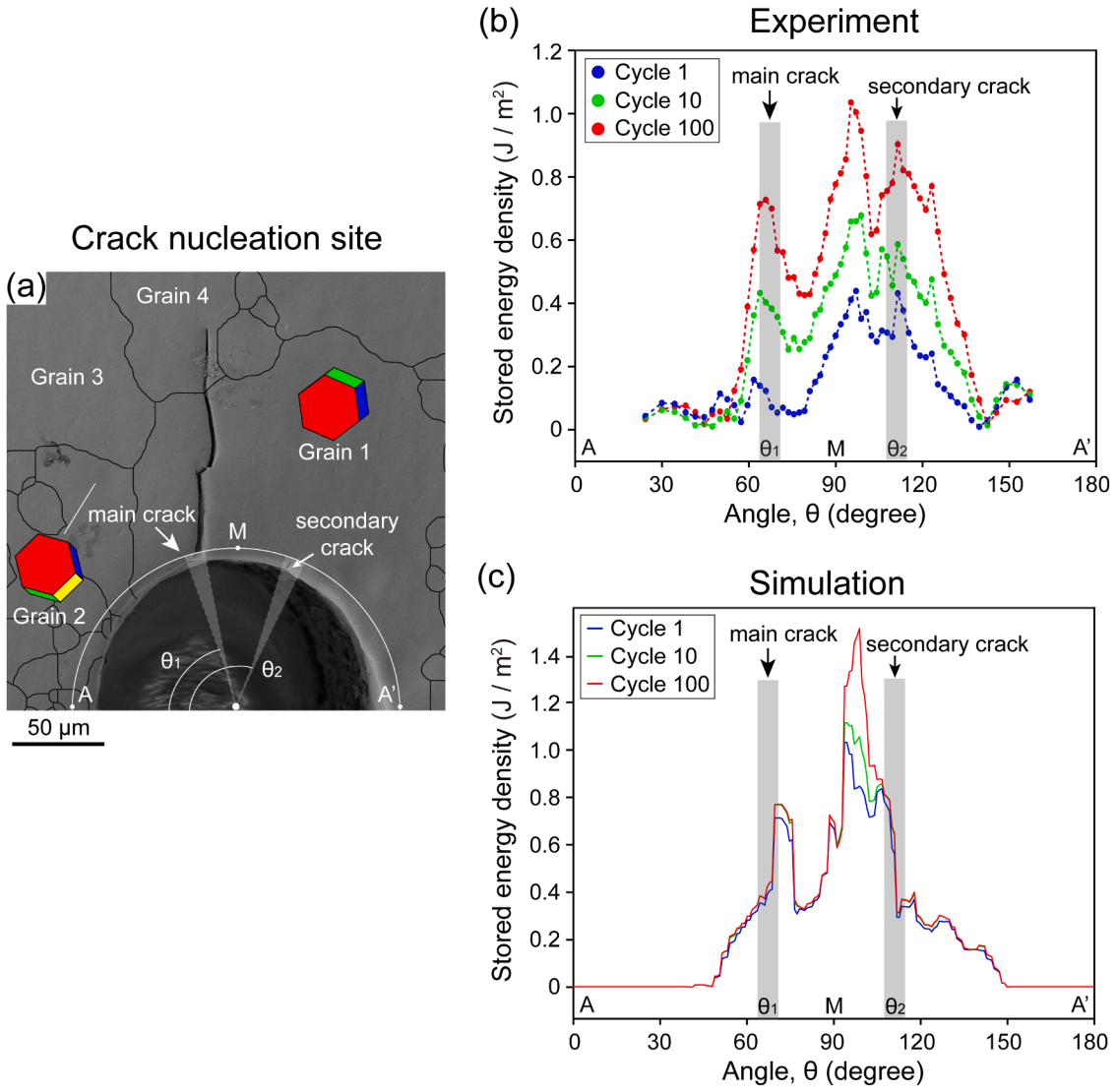


Fig. 10. (a) SEM image showing the nucleation sites of the main crack and the secondary crack corresponding to the angle theta; (b) experimental and (c) CPFE simulation results of stored energy density versus angle along path AMA' in the Zircaloy-4 sample.

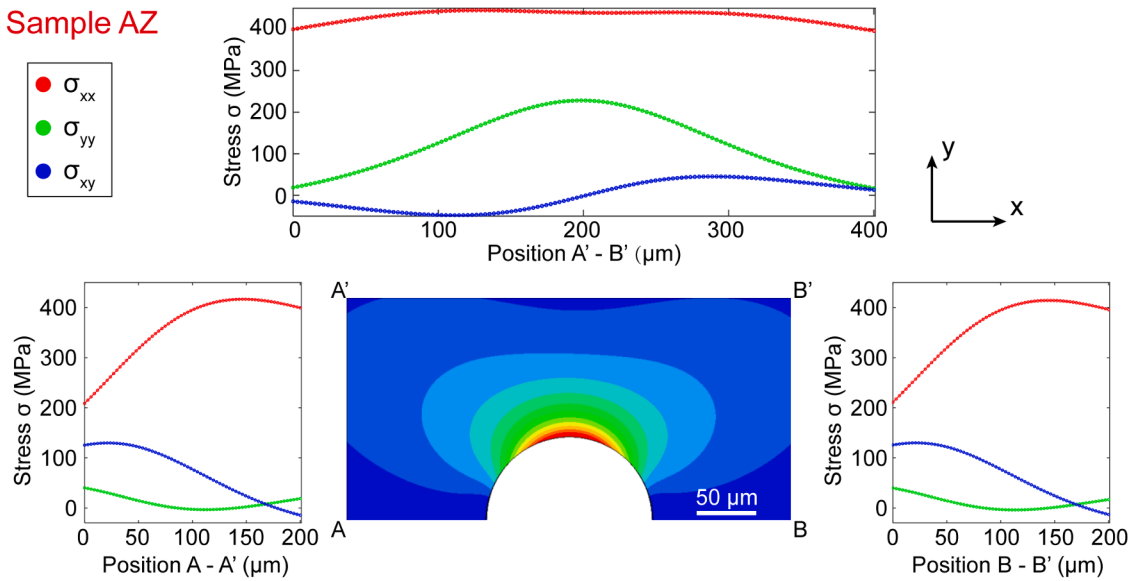


Fig. A1. The distributions of stress components along boundaries (A-A', A'-B' and B-B') for CPFE ROI sub-model in the Zircaloy-4 sample.

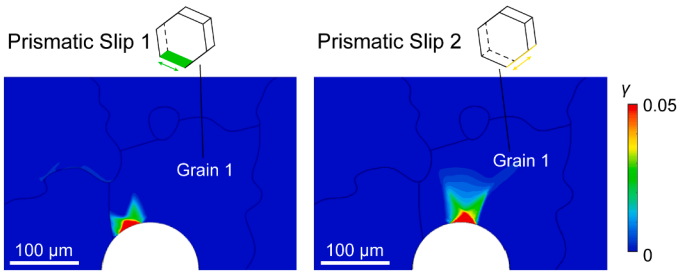


Fig. A2. CPFE results showing the activation of slip systems in the Zircaloy-4 sample.

basal texture inherited from the small-grain Zircaloy-4 plate. After 1500 cycles, a main short crack with a length of approximately 100 μm was observed, with its nucleation site located in Grain 1 and its growth path being transgranular. In addition, a secondary crack was detected at the notch root, approximately 50 μm away from the main crack nucleation site (still within Grain 1). The nucleation sites of both cracks are marked by white arrows in Fig. 5 (a) and (c). EBSD analysis enables determination of the crystallographic orientation of grains around the notch root, where crack nucleation occurs. The resulting grain orientations are depicted as hexagons, as illustrated in Fig. 5 (a).

4.2. *Local strain and stress distribution*

In-situ DIC measurement allows the local strain fields near the edge-notch of the Zircaloy-4 beam sample to be determined during the cyclic loading. CPFE modelling shows the strain distribution in the ROI focused near the notch root, which provides a full-field comparison to the experimental results. As seen in Fig. 6, the experimental and simulation results for strain (xx) at peak load and in the unloaded condition at cycle 1, cycle 10 and cycle 100 of the Zircaloy-4 sample match reasonably well. Strain (xx) in both experimental and simulation results are concentrated at the notch root and along two straight bands that form a 'wing'-shaped distribution. The strain (xx) in the unloaded condition, which is the plastic strain ignoring any residual stress, accumulates at the notch root as it increases from cycle 1 to cycle 100.

Stress concentration is expected near the notch root of the Zircaloy-4 sample during three-point bend testing. In-situ DIC measurements provide the strains at both fully applied load and in the unloaded state (as well as any other points in the cycle, if desired). This facilitates the approximate calculation of the stress distribution from in-situ DIC total strain (at full load in the cycle) and plastic strain measurements (at unload in the cycle) by estimating the difference in full-load and unload strain to give elastic strain coupled with EBSD measurement of crystallographic orientation (which is required for local anisotropic stiffness matrix determination).

Samples were cyclically loaded with stress ratio at zero such that the strain obtained in the unloaded condition is approximately equal to the plastic strain ε^p when the residual elastic strain is ignored. The strain measured at the peak load is considered to be the total strain ε^t, which is the sum of the plastic strain ε^p and the elastic strain ε^e. Thus, the elastic strain can be extracted from the difference

between the total strain and the plastic strain:

$$\boldsymbol{\varepsilon}^{e} = \boldsymbol{\varepsilon}^{t} - \boldsymbol{\varepsilon}^{p} \tag{11}$$

From Hooke's law, the stress is given by

$$\boldsymbol{\sigma} = \boldsymbol{D}\boldsymbol{\varepsilon}^{e} \tag{12}$$

where $\boldsymbol{D}$ is the (global) anisotropic stiffness matrix after rotation to account for crystallographic orientation. The rotation matrix is determined by Euler angle obtained from EBSD examination as detailed in Appendix B. Although the strain components of $\boldsymbol{\varepsilon}^{e}$ which contain the z-direction are inaccessible by two-dimensional DIC measurement, the stress tensor, $\boldsymbol{\sigma}$ can be calculated under plane stress conditions relevant to the front free surface of the sample, where $\sigma_{zz} = \sigma_{xz} = \sigma_{yz} = 0$. Thus Equation (12) can be expressed as

$$\begin{pmatrix} \sigma_{xx} \\ \sigma_{yy} \\ \sigma_{xy} \end{pmatrix} = \begin{pmatrix} D_{11} & D_{12} & D_{14} \\ D_{12} & D_{22} & D_{24} \\ D_{14} & D_{24} & D_{44} \end{pmatrix} \begin{pmatrix} \varepsilon^{e}_{xx} \\ \varepsilon^{e}_{yy} \\ \gamma^{e}_{xy} \end{pmatrix} \tag{13}$$

Then the stress tensor in plane stress can be written as

$$\sigma = \begin{pmatrix} \sigma_{xx} & \sigma_{xy} \\ \sigma_{xy} & \sigma_{yy} \end{pmatrix} \tag{14}$$

Stress components σ_{xx}, σ_{yy} and σ_{xy} are accessible by using in situ DIC measurement such that we can plot the distribution of σ_{xx}, which is instructive to represent the stress state in the ROI. Fig. 7 presents a comparison between the distribution of σ_{xx} obtained from experimental measurement and the results of CPFE modelling. The notch plays the role of stress raiser, affected also by the boundary between Grain 1 and Grain 2, which results in stress concentration in both experimental and modelling σ_{xx} distribution results.

Fig. 8 shows the variation in plastic strain (xx), ε^{p}_{xx} (strain in the unloaded condition) and σ_{xx} (stress at peak load) along the semicircle arc path AMA' for the Zircaloy-4 sample. Special care must be taken when collecting data near the notch, as the strains measured by 2D DIC are unreliable at the notch edge. Therefore, the path AMA' is defined 10 μm away radially from the notch edge and is drawn through angles 0° to 180°. Fig. 8 (a) shows the occurrence of short cracks in cycle 1500, showing the main crack and secondary crack nucleation sites marked by white arrows, which illustrates a noticeable increase in crack opening compared to the situations in cycle 1, 10, and 100. The angles in the figure can only be considered to represent the nucleation sites in a section (as indicated by the grey bands in figures (b) to (e)), taking into account the errors due to the crack opening. The main crack is located close to the angle of $\theta_1 = 70°$, while the secondary crack nucleation site is close to $\theta_2 = 110°$.

The ε^{p}_{xx} increases from cycle 1 to cycle 100, as demonstrated by the experimental results in Fig. 8 (b) and the simulation results in Fig. 8 (c). The maximum ε^{p}_{xx} recorded at cycle 100 is approximately 0.015 from experiment and 0.012 by simulation. The experimental ε^{p}_{xx} reveals two dominant peaks in proximity to the main and secondary crack nucleation sites, with a slight deviation to the left. The experimental ε^{p}_{xx} distribution along path AMA' aligns with the simulation results, both displaying two main peaks corresponding to the main and secondary crack nucleation sites, though the correlation is not exact.

The σ_{xx} at peak load obtained by experiments along path AMA' at cycle 1, cycle 10 and cycle 100 is shown in Fig. 8 (d). The simulation results (see Fig. 8 (e)) show reasonable agreement with the experimental results although more fluctuations of peak σ_{xx} are seen along path AMA' in experiment. Here, no dominant extreme of peak σ_{xx} is found to correlate with the crack nucleation site with respect to the angles, θ_1 and θ_2. Stress and plastic strain were argued to be indicators of crack nucleation site (Shanthraj and Zikry, 2013; Sweeney et al., 2013), however, as has been stated before in the literature, (plastic) strain is a necessary but not sufficient condition for crack nucleation, and stress may well be important but does not uniquely predict crack nucleation, as demonstrated in this Zircaloy-4 sample.

4.3. GND density

Metallic materials display strong size effects at the micron and sub-micron scales. Attributed to GNDs associated with non-uniform plastic deformation, this size effect is especially significant in crack nucleation as the plastic zone adjacent to the crack nucleation site may be physically small and contains large spatial gradients of deformation. During cyclic loading on a beam with an edge notch, the elastic strain is largely recovered on unload, therefore, the lattice distortion in the unloaded condition is dominated by GND development. The GND density, which is derived from plastic strain gradient, is closely tied with crystallographic slip activation. <a> prismatic slip is quantified from CPFE modelling as shown in Appendix C. Detailed microstructure information from EBSD analysis (including crystallographic orientation and grain boundary) would refine the GND density calculation by providing detailed measurement of lattice curvature, from which the former may be estimated. However, an approximate methodology is proposed to estimate measurement of the GND density magnitude based on the DIC strain analysis, which is based on that developed for crack-tip regions from the plastic strain fields measured in experiments (Xu et al., 2021).

In this study, the two-dimensional strain field in the unloaded condition is considered to comprise purely plastic contributions, considering the elasticity to be fully relaxed. The activated prismatic slip contributes very little to out-of-plane plastic strain (as a result of the texture), and are not accessible from the 2D DIC measurement. The plastic strain is given by:

$$\boldsymbol{\varepsilon}^{\mathrm{p}} = \boldsymbol{\varepsilon}^{\mathrm{Unload}} = \begin{bmatrix} \varepsilon^{\mathrm{p}}_{xx} & \varepsilon^{\mathrm{p}}_{yy} & \varepsilon^{\mathrm{p}}_{xy} \end{bmatrix}^{\mathrm{T}} \tag{15}$$

The GNDs carry the lattice curvature (Arsenlis and Parks, 1999) when material deforms inelastically and heterogeneously, and the GND density reflects the intensity of the plastic deformation gradient. Pioneering studies (Asaro, 1983; Ashby, 1970; Fleck et al., 1994; Fleck and Hutchinson, 1997) provide a one-dimensional estimation of the GND density along a single slip plane, given by:

$$\rho_{GND} = \frac{1}{b}\frac{\partial \gamma}{\partial s} \tag{16}$$

where b is the Burgers vector of the slip system, γ the shear strain and s the distance in the slip direction coordinate axis. This is generalized from Equation (16) for 2D to estimate the GND density from the incompatible plastic strain gradients available from the experimental DIC displacement measurements (to provide $\boldsymbol{F}^{\mathrm{p}}$) as follows:

$$\boldsymbol{\rho}_{\mathrm{GND}} = \frac{1}{b}(\nabla \times \boldsymbol{F}^{\mathrm{p}}) \tag{17}$$

in which $\boldsymbol{F}^{\mathrm{p}}$ is determined from the updated coordinate system. The expanded form of Equation (17) is:

$$\begin{bmatrix} \rho_{xx} & \rho_{xy} \\ \rho_{yx} & \rho_{yy} \\ \rho_{zx} & \rho_{zy} \end{bmatrix} = \frac{1}{b}\begin{bmatrix} \frac{\partial F^{\mathrm{p}}_{xx}}{\partial x} & \frac{\partial F^{\mathrm{p}}_{xx}}{\partial y} \\ \frac{\partial F^{\mathrm{p}}_{yy}}{\partial x} & \frac{\partial F^{\mathrm{p}}_{yy}}{\partial y} \\ \frac{\partial F^{\mathrm{p}}_{xy}}{\partial x} & \frac{\partial F^{\mathrm{p}}_{xy}}{\partial y} \end{bmatrix} \tag{18}$$

By virtue of minimizing the dislocation energy (Kysar et al., 2010), the scalar of effective GND density is given as the sum of the 2nd order norm of its components (Cheng and Ghosh, 2015):

$$\rho_{\mathrm{GND}} = \left(\sum_{j=1}^{2} \sum_{i=1}^{3} \rho_{ij} \right)^{1/2} \tag{19}$$

The <a> prismatic slip Burgers vector ($b = 0.323$ nm) is applied. The algorithm for determining the GND density assumes that the DIC region is a single phase, single crystal microstructure, and that all slip systems share the same Burgers vector magnitude.

The GND density along path AMA' at cycle 1, cycle 10 and cycle 100 has been quantified versus angle and is shown in Fig. 9 for both experimental results (a) and simulation results (b). The CPFE modelling results show agreement with the magnitude of the GND density estimated in experiments. However, the distribution of GND density in the simulation results show much sharper peaks near the notch root. This arises from the localised stress states and from dislocations tending to exit from the sample notch free surface, which is analogous to the phenomenon of a dislocation free zone (Chang and Ohr, 1981) that has been both experimentally observed (Wilkinson et al., 2006) and rationalized in recent crystal plasticity simulations (Xu, 2021).

GND density has been shown not only to strengthen the mechanical response, but also to be one of the factors determining fatigue crack nucleation in ductile materials (e.g. Prastiti et al.,2020), as the GNDs reflects the strain gradients and carries local lattice curvature (Arsenlis and Parks, 1999). In the present study, the experimental characterisation and simulation prediction of peak GND densities do not show strong correlation with the fatigue crack nucleation sites (indicated as the grey region in Fig. 9) along the notch of the specimen, but nonetheless contribute to the distributions of stored energy density.

4.4. Stored energy density

Stored energy density is calculated both from the experimental measurements of local stress, plastic strain and GND density, and directly within the CPFE model for comparison. For the experimental estimation, it is argued that $\rho_{GND} \gg \rho_{SSD}$ when there is large lattice distortion near the notch root, such that the contribution of ρ_{SSD} to the total dislocation density can be neglected when a cyclic loading with a stress ratio of R = 0 is applied. Therefore, the stored energy density can be calculated approximately by simplifying Equation 10

$$G \approx \int \frac{\left| \xi \boldsymbol{\sigma} : d\boldsymbol{\epsilon}_{\mathrm{p}} \right|}{\sqrt{\rho_{GND}}} \tag{20}$$

As the local stress tensor, local plastic strain tensor and GND density have been experimentally measured, the stored energy density can be calculated from Equation (20) using these experimental results. Fig. 10 shows the variation of stored energy density along path AMA' as a function of angle (θ). The CPFE simulation results of stored energy density are in reasonably good agreement with the experimental results, with three peaks detected along path AMA' in both the experimental and simulation results (ignoring some small peaks) as shown in Fig. 10 (b) and (c). Two significant peaks of stored energy density in the experimental results close to $\theta_1 = 70^\circ$ and $\theta_2 = 110^\circ$ indicate the main crack nucleation site and the secondary nucleation site, respectively, suggesting that the stored energy density distribution reflects aspects of the observed crack nucleation sites. However, the highest value of stored energy density is detected near Point M, where no crack nucleation is observed.

The results of the CPFE modelling exhibit a degree of agreement between the stored energy density that aligns relatively closely with the values derived from experimental studies, demonstrating an approximate stored energy density of about 0.8 J/m^2 proximate to the primary crack nucleation site at cycle 100. Although the simulated stored energy density's maximum, estimated at approximately 1.5 J/m^2, surpasses the experimental peak stored energy (1.0 J/m^2), it remains within the same order of magnitude.

5. Conclusions

A textured Zircaloy-4 sample was tested under cyclic load in which fatigue crack nucleation was examined at the notch root, where a main and secondary crack were found to nucleate and grow transgranularly.

In-situ DIC was used to measure strain distributions near the crack nucleation sites, coupled with EBSD orientation data to facilitate calculation of local stresses. CPFE modelling provided comparisons of the distribution and magnitudes of local strain, and stress. A deformation-gradient-tensor based method was utilised to calculate the GND density from experimentally measured strains and coupling of DIC strain measurement with EBSD crystallographic examination. The CPFE modelling results of GND density capture the magnitude of the experimental measurements.

Stored energy density was determined using both experiment and simulation, with knowledge of local plastic strain, stress and dislocation density. The CPFE results for stored energy density were in reasonable agreement with the experimental results. The hotspots of both experimental and simulated stored energy densities (with the exception of the central peak value) identify the main crack and secondary crack nucleation sites, underscoring the stored energy density as a reliable predictor for fatigue crack nucleation.

Appendices

Appendix A. The distributions of the major stress components along the three boundaries for the crystal plasticity ROI sub-model in the Zircaloy-4 sample Fig. A1

Appendix B. Rotation matrices mapping the reference crystal system into the local system for specified crystallographic orientation Fig. A2

The convention of the ZXZ rotation with the Euler angle, (φ_1 Φ φ_2) is: i) Rotate through φ_1 about the z-axis; ii) Rotate through Φ about the (new) x'-axis; iii) Rotate through φ_2 about the (new) z''-axis. Simply, this can be expressed as

$$\boldsymbol{R} = \boldsymbol{R}(\varphi_2)\boldsymbol{R}(\Phi)\boldsymbol{R}(\varphi_1)$$

where

$$\boldsymbol{R} = \begin{pmatrix} cos\varphi_2 & -sin\varphi_2 & 0 \\ sin\varphi_2 & cos\varphi_2 & 0 \\ 0 & 0 & 1 \end{pmatrix} \begin{pmatrix} 1 & 0 & 0 \\ 0 & cos\Phi & -sin\Phi \\ 0 & sin\Phi & cos\Phi \end{pmatrix} \begin{pmatrix} cos\varphi_1 & -sin\varphi_1 & 0 \\ sin\varphi_1 & cos\varphi_1 & 0 \\ 0 & 0 & 1 \end{pmatrix}$$

which can be written out as

$$\boldsymbol{R} = \begin{pmatrix} R_{11} & R_{12} & R_{13} \\ R_{21} & R_{22} & R_{23} \\ R_{31} & R_{32} & R_{33} \end{pmatrix}$$

To fulfil the rotation of stiffness matrix, $\boldsymbol{T}_{\boldsymbol{\sigma}}$ and $\boldsymbol{T}_{\boldsymbol{\varepsilon}}$ are the relevant rotation matrices for the stress and strain column vectors respectively with

$$\boldsymbol{\sigma}' = \boldsymbol{T}_{\boldsymbol{\sigma}}\boldsymbol{\sigma}$$

$$\boldsymbol{\varepsilon}' = \boldsymbol{T}_{\boldsymbol{\varepsilon}}\boldsymbol{\varepsilon}$$

where

$$= \boldsymbol{R}(\varphi_2)\boldsymbol{R}(\Phi)\boldsymbol{R}(\varphi_1)$$

and

$$\rho_{\mathrm{GND}} = \left(\sum_{j=1}^{2} \sum_{i=1}^{3} \rho_{ij} \right)^{1/2}$$

Appendix C. Activation of slip systems

Declaration of Competing Interest

The authors declare that they have no known competing financial interests or personal relationships that could have appeared to

influence the work reported in this paper.

Data availability

Data will be made available on request.

Acknowledgments

WW thanks the support from the National Natural Science Foundation of China. YX and FPED acknowledge the financial support by the Engineering and Physical Sciences Research Council for funding through the grant EP/R018863/1. FPED wishes to acknowledge gratefully the provision of Royal Academy of Engineering/Rolls-Royce research chair funding.

Credit author statement

Weifeng Wan: Experiment, Methodology, Original draft preparation, Formal analysis
Yilun Xu: Conceptualization, Methodology, Modelling, Original draft preparation, Visualization
Xikai Yu: Modelling, Formal analysis
Fionn Dunne: Conceptualization, Methodology, Writing- Reviewing and Editing, Supervision

References

Arsenlis, A., Parks, D.M., 1999. Crystallographic aspects of geometrically-necessary and statistically-stored dislocation density. Acta Mater. 47, 1597–1611. https://doi.org/10.1016/S1359-6454(99)00020-8.
Asaro, R.J., 1983. Crystal plasticity. J. Appl. Mech. Trans. ASME 50, 921–934. https://doi.org/10.1115/1.3167205.
Ashby, M.F., 1970. The deformation of plastically non-homogeneous materials. Philos. Mag. 21, 399–424. https://doi.org/10.1080/14786437008238426.
Bergsmo, A., Xu, Y., Poole, B., Dunne, F.P., 2022. Twin boundary fatigue crack nucleation in a polycrystalline Nickel superalloy containing non-metallic inclusions. J. Mech. Phys. Solids 160, 104785. https://doi.org/10.1016/j.jmps.2022.104785.
Brinckmann, S., Van der Giessen, E., 2004. A discrete dislocation dynamics study aiming at understanding fatigue crack initiation. Mater. Sci. Eng. A 461–464. https://doi.org/10.1016/j.msea.2004.01.142, 387–389.
Brown, L.M., 2013. Cracks and extrusions caused by persistent slip bands. Philos. Mag. 93, 3809–3820. https://doi.org/10.1080/14786435.2013.798048.
Castelluccio, G.M., Musinski, W.D., McDowell, D.L., 2014. Recent developments in assessing microstructure-sensitive early stage fatigue of polycrystals. Curr. Opin. Solid State Mater. Sci. 18, 180–187. https://doi.org/10.1016/j.cossms.2014.03.001.
Chen, B., Jiang, J., Dunne, F.P.E., 2018. Is stored energy density the primary meso-scale mechanistic driver for fatigue crack nucleation? Int. J. Plast. 101, 213–229. https://doi.org/10.1016/j.ijplas.2017.11.005.
Chang, S.J., Ohr, S.M., 1981. Dislocation-free zone model of fracture. J. Appl. Phys. 52, 7174–7181. https://doi.org/10.1063/1.328692.
Chen, B., Jiang, J., Dunne, F.P.E., 2017. Microstructurally-sensitive fatigue crack nucleation in Ni-based single and oligo crystals. J. Mech. Phys. Solids 106, 15–33. https://doi.org/10.1016/j.jmps.2017.05.012.
Cheng, A.S., Laird, C., 1981. Fatigue life behavior of copper single crystals. part i: observations of crack nucleation. Fatigue Fract. Eng. Mater. Struct. 4, 331–341. https://doi.org/10.1111/j.1460-2695.1981.tb01130.x.
Cheng, J., Ghosh, S., 2015. A crystal plasticity FE model for deformation with twin nucleation in magnesium alloys. Int. J. Plast. 67, 148–170. https://doi.org/10.1016/j.ijplas.2014.10.005.
Cottrell, A.H., Hull, D., 1957. Extrusion and intrusion by cyclic slip in copper. Proc. R. Soc. London. Ser. A. Math. Phys. Sci. 242, 211–213. https://doi.org/10.1098/rspa.1957.0170.
Dunne, F.P.E., 2014. Fatigue crack nucleation: mechanistic modelling across the length scales. Curr. Opin. Solid State Mater. Sci. 18, 170–179. https://doi.org/10.1016/j.cossms.2014.02.005.
Dunne, F.P.E., Rugg, D., Walker, A., 2007a. Lengthscale-dependent, elastically anisotropic, physically-based hcp crystal plasticity: application to cold-dwell fatigue in Ti alloys. Int. J. Plast. 23, 1061–1083. https://doi.org/10.1016/j.ijplas.2006.10.013.
Dunne, F.P.E., Wilkinson, A.J., Allen, R., 2007b. Experimental and computational studies of low cycle fatigue crack nucleation in a polycrystal. Int. J. Plast. 23, 273–295. https://doi.org/10.1016/j.ijplas.2006.07.001.
Fatemi, A., Socie, D.F., 1988. A critical plane approach to multiaxial fatigue damage including out-of-phase loading. Fatigue Fract. Eng. Mater. Struct. 11, 149–165. https://doi.org/10.1111/j.1460-2695.1988.tb01169.x.
Fleck, N.A., Hutchinson, J.W., 1997. Strain Gradient Plasticity. Adv. Appl. Mech. 33, 295–361. https://doi.org/10.1016/S0065-2156(08)70388-0.
Fleck, N.A., Muller, G.M., Ashby, M.F., Hutchinson, J.W., 1994. Strain gradient plasticity: theory and experiment. Acta Metall. Mater. 42, 475–487. https://doi.org/10.1016/0956-7151(94)90502-9.
Forsyth, P.J.E., 1953. Exudation of material from slip bands at the surface of fatigued crystals of an Aluminium-Copper alloy. Nature 171, 172–173.
Griffith, A.A., 1921. The phenomena of rupture and flow in solids. Philos. Trans. R. Soc. A Math. Phys. Eng. Sci. 221, 163–198.
Ho, H.S., Risbet, M., Feaugas, X., 2015. On the unified view of the contribution of plastic strain to cyclic crack initiation: impact of the progressive transformation of shear bands to persistent slip bands. Acta Mater. 85, 155–167. https://doi.org/10.1016/j.actamat.2014.11.020.
Hochhalter, J.D., Littlewood, D.J., Christ, R.J., Veilleux, M.G., Bozek, J.E., Ingraffea, A.R., Maniatty, A.M., 2010. A geometric approach to modeling microstructurally small fatigue crack formation: II. Physically based modeling of microstructure-dependent slip localization and actuation of the crack nucleation mechanism in AA 7075-T651. Model. Simul. Mater. Sci. Eng. 18 https://doi.org/10.1088/0965-0393/18/4/045004.
Jiang, J., Zhang, T., Dunne, F.P.E., Britton, T.Ben, 2016. Deformation compatibility in a single crystalline Ni superalloy. Proc. R. Soc. A Math. Phys. Eng. Sci. 472 https://doi.org/10.1098/rspa.2015.0690.
Kysar, J.W., Saito, Y., Oztop, M.S., Lee, D., Huh, W.T., 2010. Experimental lower bounds on geometrically necessary dislocation density. Int. J. Plast. 26, 1097–1123. https://doi.org/10.1016/j.ijplas.2010.03.009.
Littlewood, P.D., Wilkinson, A.J., 2012. Geometrically necessary dislocation density distributions in cyclically deformed Ti-6Al-4V. Acta Mater 60, 5516–5525. https://doi.org/10.1016/j.actamat.2012.07.003.
Liu, Y., Wan, W., Dunne, F.P.E., 2022. Characterisation and modelling of micro- and macroscale creep and strain rate sensitivity in Zircaloy-4. Mater. Sci. Eng. A 840, 142981. https://doi.org/10.1016/j.msea.2022.142981.
Man, J., Obrtlík, K., Polák, J., 2009. Extrusions and intrusions in fatigued metals. Part 1. State of the art and history. Philos. Mag. 89, 1295–1336. https://doi.org/10.1080/14786430902917616.
Manonukul, A., Dunne, F.P.E., 2004. High- and low- cycle fatigue crack initiation using polycrystal plasticity. Proc. R. Soc. A Math. Phys. Eng. Sci. 460, 1881–1903.

Miao, J., Pollock, T.M., Wayne Jones, J., 2012. Microstructural extremes and the transition from fatigue crack initiation to small crack growth in a polycrystalline nickel-base superalloy. Acta Mater. 60, 2840–2854. https://doi.org/10.1016/j.actamat.2012.01.049.
Nielsen, R.H., Wilfing, G., 2012. Zirconium and zirconium compounds. 10.1002/14356007.a28.
Nye, F., 1953. Some geometrical relations in dislocated crystals. Acta Metall 1.
Pineau, A., McDowell, D.L., Busso, E.P., Antolovich, S.D., 2016. Failure of metals II: fatigue. Acta Mater. 107, 484–507. https://doi.org/10.1016/j.actamat.2015.05.050.
Prastiti, N.G., Xu, Y., Balint, D.S., Dunne, F.P.E., 2020. Discrete dislocation, crystal plasticity and experimental studies of fatigue crack nucleation in single-crystal nickel. Int. J. Plast. 126, 102615 https://doi.org/10.1016/j.ijplas.2019.10.003.
Przybyla, C.P., McDowell, D.L., 2011. Simulated microstructure-sensitive extreme value probabilities for high cycle fatigue of duplex Ti-6Al-4V. Int. J. Plast. 27, 1871–1895. https://doi.org/10.1016/j.ijplas.2011.01.006.
Przybyla, C.P., Musinski, W.D., Castelluccio, G.M., McDowell, D.L., 2013. Microstructure-sensitive HCF and VHCF simulations. Int. J. Fatigue 57, 9–27. https://doi.org/10.1016/j.ijfatigue.2012.09.014.
Sangid, M.D., Maier, H.J., Sehitoglu, H., 2011. A physically based fatigue model for prediction of crack initiation from persistent slip bands in polycrystals. Acta Mater 59, 328–341. https://doi.org/10.1016/j.actamat.2010.09.036.
Sauzay, M., Gilormini, P., 2002. Influence of surface effects on fatigue of microcracks nucleation. Theor. Appl. Fract. Mech. 38, 53–62. https://doi.org/10.1016/S0167-8442(02)00080-0.
Shanthraj, P., Zikry, M.A., 2013. Microstructurally induced fracture nucleation and propagation in martensitic steels. J. Mech. Phys. Solids 61, 1091–1105. https://doi.org/10.1016/j.jmps.2012.11.006.
Stroh, A.N., 1954. The formation of cracks as a result of plastic flow. Proc. R. Soc. A Math. Phys. Eng. Sci. 223, 404–414. https://doi.org/10.1098/rspa.1954.0124.
Stroh, A.N., 1953. A theoretical calculation of the stored energy in a work-hardened material. Proc. R. Soc. London. Ser. A. Math. Phys. Sci. 218, 391–400. https://doi.org/10.1098/rspa.1953.0112.
Suresh, S., 1998. Fatigue of Materials. Cambridge University Press, Cambridge. https://doi.org/10.1017/cbo9780511806575.
Suresh, S., Ritchie, R.O., 1984. Propagation of short fatigue cracks. Int. Met. Rev. 29, 445–473. https://doi.org/10.1179/imtr.1984.29.1.445.
Sweeney, C.A., Vorster, W., Leen, S.B., Sakurada, E., McHugh, P.E., Dunne, F.P.E., 2013. The role of elastic anisotropy, length scale and crystallographic slip in fatigue crack nucleation. J. Mech. Phys. Solids 61, 1224–1240. https://doi.org/10.1016/j.jmps.2013.01.001.
Szczepanski, C.J., Jha, S.K., Shade, P.A., Wheeler, R., Larsen, J.M., 2013. Demonstration of an in situ microscale fatigue testing technique on a titanium alloy. Int. J. Fatigue 57, 131–139. https://doi.org/10.1016/j.ijfatigue.2012.08.008.
Tanaka, K., Mura, T., 1982. A micromechanical theory of fatique crack initiation from notches. Mech. Mater. 1, 63–73. https://doi.org/10.1016/0167-6636(82)90024-2.
Thompson, N., Wadsworth, N., Louat, N., 1956. The origin of fatigue fracture in copper. Philos. Mag. 1, 113–126. https://doi.org/10.1080/14786435608238086.
Wan, V.V.C., Jiang, J., MacLachlan, D.W., Dunne, F.P.E., 2016. Microstructure-sensitive fatigue crack nucleation in a polycrystalline Ni superalloy. Int. J. Fatigue 90, 181–190. https://doi.org/10.1016/j.ijfatigue.2016.04.013.
Wan, V.V.C., Maclachlan, D.W., Dunne, F.P.E., 2014. A stored energy criterion for fatigue crack nucleation in polycrystals. Int. J. Fatigue 68, 90–102. https://doi.org/10.1016/j.ijfatigue.2014.06.001.
Wilkinson, A.J., Meaden, G., Dingley, D.J., 2006. High resolution mapping of strains and rotations using electron backscatter diffraction. Mater. Sci. Technol. 22, 1271–1278. https://doi.org/10.1179/174328406X130966.
Wilson, D., Zheng, Z., Dunne, F.P.E., 2018. A microstructure-sensitive driving force for crack growth. J. Mech. Phys. Solids 121, 147–174. https://doi.org/10.1016/j.jmps.2018.07.005.
Wood, W.A., 1958. Formation of fatigue cracks. Philos. Mag. 3, 692–699. https://doi.org/10.1080/14786435808237004.
Xu, Y., 2021. A non-local methodology for geometrically necessary dislocations and application to crack tips. Int. J. Plast. 140, 102970. https://doi.org/10.1016/j.ijplas.2021.102970.
Xu, Y., Wan, W., Dunne, F.P.E., 2021. Microstructural fracture mechanics: stored energy density at fatigue cracks. J. Mech. Phys. Solids 146, 104209. https://doi.org/10.1016/j.jmps.2020.104209.